Microscopic dynamics of stress relaxation in a nanocolloidal soft glass

Yihao Chen,[1] Simon A. Rogers,[2] Suresh Narayanan,[3] James L. Harden,[4] and Robert L. Leheny[1]
[1]*Department of Physics and Astronomy, Johns Hopkins University, Baltimore, Maryland 21218, USA*
[2]*Department of Chemical and Biomolecular Engineering, University of Illinois Urbana-Champaign, Champaign, Illinois 61801, USA*
[3]*X-Ray Science Division, Argonne National Laboratory, Argonne, Illinois 60439, USA*
[4]*Department of Physics & CAMaR, University of Ottawa, Ottawa, Ontario, Canada K1N 6N5*

(Received 1 March 2019; accepted 19 February 2020; published 6 March 2020)

We report x-ray photon correlation spectroscopy (XPCS) experiments with *in situ* rheometry performed on a soft glass composed of a concentrated suspension of charged silica nanoparticles subjected to step strains that induce yielding and flow. The XPCS measurements characterize the particle-scale and mesoscale motions within the glass that underlie the highly protracted decay of the macroscopic stress following the step strains. These dynamics are anisotropic, with slow, convective particle motion along the direction of the preceding shear that persists for surprisingly large times and that is accompanied by intermittent motion in the perpendicular (vorticity) direction. A close correspondence between the convective dynamics and stress relaxation is demonstrated by power-law scaling between the characteristic velocity of the collective particle motion and the rate of stress decay.

DOI: 10.1103/PhysRevMaterials.4.035602

I. INTRODUCTION

Many soft amorphous solids behave as yield-stress materials that flow when subjected to sufficiently large applied force but return to a solid when the force is removed [1]. The nature of this fluid-solid transition is fundamental to the out-of-equilibrium state of glassy materials and its dependence on sample history, and it plays a key role in prominent theoretical ideas about glasses such as jamming and soft glassy rheology [2–4]. Further, since processing amorphous solids often involves inducing flow, the manner in which the materials regain solidlike properties following flow cessation is important for their utility in applications. When flow ceases, soft amorphous solids typically display a protracted recovery during which stress at fixed applied strain slowly decreases to a value, known as the residual stress, that can depend on aspects of the preceding flow such as the shear rate and the total magnitude of the strain [4–16]. While numerous rheology studies have characterized the macroscopic nature of stress relaxation, little is known experimentally about the underlying microscopic structural dynamics.

Identifying such microstructural changes connected to macroscopic deformation and flow is a central challenge for the fields of soft matter and colloid science [17]. To address this problem, a number of recent studies have combined microscopy or scattering methods in concert with rheometry to probe the microscopic signatures of various aspects of the nonlinear rheological behavior of colloidal glasses. Such studies have included investigations of the particle-scale rearrangements associated with yielding under start-up shear [18,19] and large-amplitude oscillatory shear [20–23], studies connecting the microscopic and macroscopic manifestations of slip [24], and experiments probing the dynamics associated with creep [25] and precursors to failure [26] under steady applied stress. However, to our knowledge no such previous work has considered the microscopic dynamics associated with stress relaxation at fixed macroscopic strain. In this paper we report x-ray photon correlation spectroscopy (XPCS) measurements that track particle-scale motion in a nanocolloidal soft glass following cessation of shearing and compare these dynamics with the time-dependent stress measured with *in situ* rheometry.

The experiments focus on the dynamics that occur after the glass has been strained to points near and above yielding. The XPCS results reveal anisotropic dynamics that are qualitatively different along the direction of the preceding shear (i.e., the flow direction) and along the perpendicular (vorticity) direction. In the direction of the preceding shear, the dynamics are characterized by convective-like particle motion that slows steadily with time but that persists for surprisingly large times. An intimate connection between these convective dynamics and the stress relaxation is demonstrated by power-law scaling between the characteristic velocity of the particle motion and the rate of stress decay. Accompanying this convective "back flow" is highly intermittent motion in the vorticity direction that has the character of avalanches. These observations, which contrast with prevailing pictures of the dynamics in soft glasses that describe stress relaxation in terms of local particle rearrangements, suggest a new theoretical perspective is needed to understand the phenomenon.

II. MATERIALS AND METHODS

A. Soft glass preparation and characteristics

The ductile soft glass was composed of Ludox TM-50 (Sigma Aldrich), which are charge-stabilized silica nanospheres, in water [27]. The average colloid radius was 13.3 nm with a standard deviation of 1.4 nm, as determined from fits of the x-ray form factor measured on a dilute suspension of the colloids. The glass was formed from a suspension with initial colloid volume fraction of approximately 0.3 and

with 50 mM salt, according to the manufacturer's specifications. 25 mL of the suspension were centrifuged at 48 000 g for 30 minutes, and the supernatant was poured off, leaving a solid plug of material. The plug was gently mixed to remove concentration gradients and then was centrifuged at 2000 g for 5 minutes to remove any air bubbles introduced by stirring. A 0.5 mL section was extracted from the center of the plug for the rheo-XPCS experiments. Following the experiments, a portion of the sample was weighed, then dried and reweighed, to measure the solid fraction, which corresponded a colloidal volume fraction of $\phi = 0.43$, assuming a silica density of 2 g/cm^3.

Previous work by Philippe *et al.* on concentrated suspensions of Ludox TM-50 nanoparticles identified the transition between a "supercooled" colloidal liquid at lower ϕ and an out-of-equilibrium glass at higher ϕ near $\phi_g \approx 0.40$ [27]. Notably, this volume fraction is significantly below that of the hard-sphere glass transition, $\phi_g^{\rm hs} \approx 0.58$, implying the charged nanocolloids form the glassy phase primarily by virtue of the soft repulsion created by the screened Coulomb potential [27]. Hence, the suspension employed in our experiments with $\phi = 0.43$ can be described as nanocolloidal soft glass.

B. Rheo-XPCS

The rheo-XPCS experiments were carried out at Sector 8-ID of the Advanced Photon Source. The sample was contained in a Couette cell of a stress-controlled rheometer (Anton Paar MCR 301) mounted on the beam line, enabling rheological tests in parallel with x-ray scattering measurements. A 10.9 keV, partially coherent x-ray beam of size $100 \times 20 \mu$m^2 (V x H) was focused vertically to a 3×20 μm^2 spot on the sample. An area detector (X-spectrum LAMBDA 750 K) [28,29] 4.91 m after the sample measured the scattering intensity over wave vectors 0.06 nm^{-1} $< |\mathbf{q}| <$ 0.65 nm^{-1}. The Couette cell was composed of thin-walled polycarbonate with inner and outer diameters of 11.0 and 11.4 mm, respectively. Measurements were performed with the axis of the Couette cell oriented vertically and the horizontal incident beam directed radially through the center of the cell so that the incident beam was parallel to the shear-gradient (Δ) direction. In the small-angle scattering regime, where the scattering wave vector is essentially perpendicular to the incident wave vector, $\mathbf{q}$ was hence in the flow-vorticity (v-ω) plane.

Figure 1(a) shows the stress σ as a function of applied strain γ during shear of the glass at a strain rate $\dot{\gamma} = 0.01$ s^{-1}. The data contain features common to yield-stress materials. Above the linear elastic regime at small strain, the stress goes through an "overshoot" near $\gamma = 5\%$ that is a characteristic of yielding. At larger strain, σ becomes roughly independent of γ, indicating viscoplastic flow. In each stress relaxation measurement, the glass was first held at zero applied stress for an extended period and was then subjected to steady shear at strain rate $\dot{\gamma} = 0.01$ s^{-1} from zero initial strain until a desired strain γ was reached. The strain was then fixed, and the stress required to hold γ constant was monitored as a function of waiting time t. Strains at which measurements were performed, indicated by arrows in Fig. 1(a), ranged from $\gamma =$ 2%, which is in the linear elastic regime, to $\gamma = 20\%$, which is in the regime of viscoplastic flow. The time-dependent stress

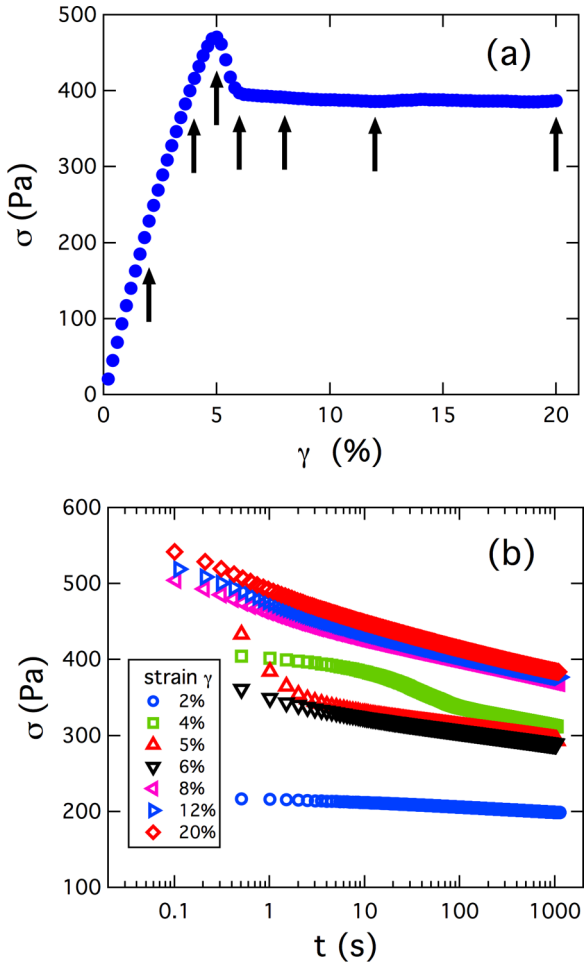

FIG. 1. (a) Stress as a function of strain during startup shear at $\dot{\gamma} = 0.01$ s^{-1}. The arrows indicate the strain values at which shear was stopped and strain held fixed in the stress relaxation measurements. (b) Stress as a function of waiting time with strain held at these various values following a step from zero strain at strain rate $\dot{\gamma} = 0.01$ s^{-1}.

following the steps to each γ is shown in Fig. 1(b). In all cases, σ displayed a protracted, quasi-logarithmic decay that extended beyond the measurement time of 1000 s. (The rheo-XPCS measurements were conducted over two days during which the rheology evolved slightly, due either to aging of the soft glass [27] or possibly to a small amount of evaporation of water from the sample. Specifically, the linear shear modulus varied from 10.3 to 16 kPa. Hence, the exact magnitudes of the stress at different strains in Fig. 1(b) should not be compared).

During the step strains and subsequent stress relaxation at fixed γ, a series of coherent x-ray images, or "speckle patterns," was obtained at 10 fps for 10 000 frames to characterize the microscopic dynamics. Additional measurements at $\gamma = 5\%$ and 6% at 100 fps for 10 000 frames captured the dynamics at higher temporal resolution immediately following the step strains. Figure 2(a) shows an example scattering pattern captured by the area detector during a measurement at 10 fps. Figure 2(b) shows the scattering intensity $I(q)$, averaged over 10 000 frames and averaged over wave-vector directions, as a function of the wave-vector magnitude q. The

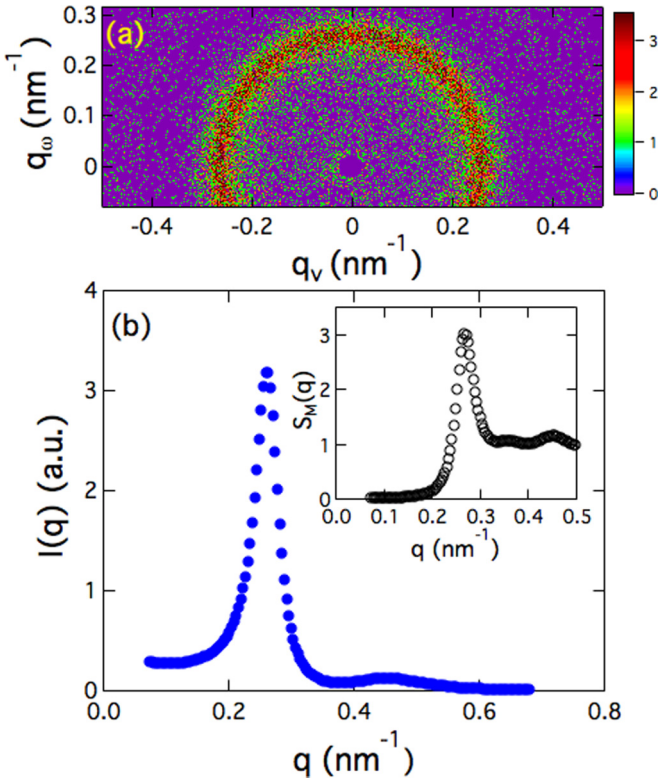

FIG. 2. (a) Example area-detector image of the scattering pattern during a measurement at 10 fps. The signal is expressed as the number of photons detected by each pixel of the detector. The small circular region with zero scattering near $q = 0$ is the shadow of the beam stop. (b) Scattering intensity I averaged over wave-vector direction as a function of the wave-vector magnitude q. The intensity is an average over 10 000 frames. The inset to (b) shows the measurable structure factor $S_M(q)$ determined from $S_M(q) = I(Q)/F(q)$, where $F(q)$ is the measured form factor.

inset to Fig. 2(b) shows the "measurable" structure factor $S_M(q)$ obtained from $S_M(q) = I(q)/F(q)$, where $F(q)$ is the form factor measured on a dilute suspension of the Ludox TM-50 particles. We note $S_M(q)$ only approximates the true structure factor due to the polydispersity in particle size [30]. The primary feature in $S_M(q)$ is a structure factor peak near $q = 0.26$ nm^{-1} typical of a colloidal glass.

III. RESULTS AND DISCUSSION

A. Dynamics along the strain direction: Convective "backflow"

The microscopic dynamics captured by the XPCS measurements during the stress relaxation showed strong dependence on waiting time and direction that is captured by the instantaneous correlation function [31],

$$C(\mathbf{q}, t_1, t_2) = \frac{\langle I(\mathbf{q}, t_1) I(\mathbf{q}, t_2)\rangle}{\langle I(\mathbf{q}, t_1)\rangle \langle I(\mathbf{q}, t_2)\rangle}, \quad (1)$$

where $I(\mathbf{q}, t)$ is the scattering intensity at wave vector $\mathbf{q}$ and time t, and the brackets indicate averages over detector pixels within a small vicinity of $\mathbf{q}$. Figure 3 shows the instantaneous correlation function during stress relaxation with $\gamma = 6\%$ at a wave vector parallel to the initial strain, $q_v = 0.26$ nm^{-1},

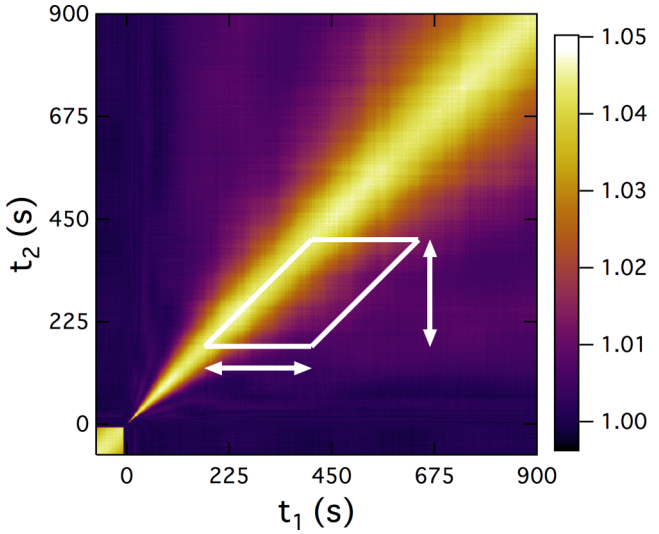

FIG. 3. Instantaneous correlation function $C(q_v, t_1, t_2)$ during a stress relaxation measurement following a step to $\gamma = 6\%$ measured at $q_v = 0.26$ nm^{-1} along the direction of the initial strain. The white parallelogram indicates the region employed in calculating the autocorrelation function at $t = 293$ s. The arrows, indicating the size of the region, span 171 s $< t_{1,2} <$ 415 s.

near the first peak in the structure factor. The time when γ reached 6% ($t = 0$) is taken as the origin in Fig. 3. Preceding the step strain, the dynamics in the quiescent glass were arrested. Consequently, pairs of speckle patterns taken before the step (i.e., both $t_1 < 0$ and $t_2 < 0$) are highly similar, and $C(q_v, t_1, t_2)$ is large and effectively constant at a value near $bf_\infty + 1$, where $b \approx 0.055$ is the Siegert factor [32], and f_∞ is the wave-vector-dependent nonergodicity parameter [33] plotted in Fig. 4. Shortly following the step, $C(q_v, t_1, t_2)$ is significantly larger than one only near the diagonal corresponding to small time differences $|t_1 - t_2|$, indicating the step

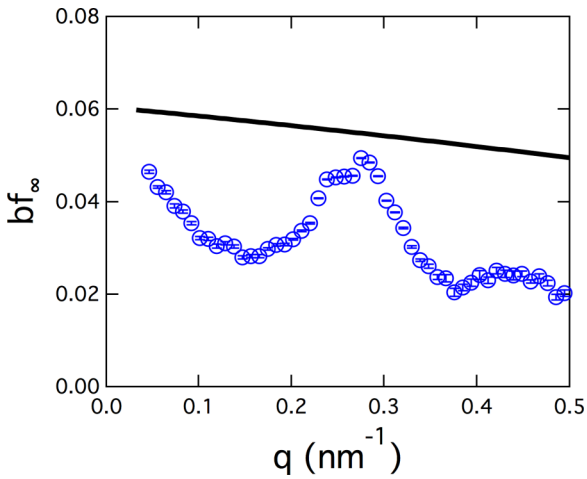

FIG. 4. The product bf_∞ (symbols) obtained from the amplitude of the XPCS correlation function, $g_2(\mathbf{q}, \tau) - 1$, at small τ measured on the soft glass. The line shows the Siegert factor b obtained from a separate XPCS measurement on a thin aerogel sample [32]. The wave-vector-dependent nonergodicity parameter f_∞ is a measure of the fourier components of the arrested concentration fluctuations in the glass [33].

strain induced subsequent particle dynamics that were initially rapid. With increasing waiting time the dynamics steadily slowed, and correlations persist for progressively larger time differences such that the band of large $C(q_v, t_1, t_2)$ values along the diagonal broadens.

To analyze these dynamics quantitatively, we obtain the more familiar normalized autocorrelation functions $\Delta g_2(q_v, \tau; t)$ by averaging $C(q_v, t_1, t_2)$ at fixed delay time $\tau = |t_1 - t_2|$,

$$\Delta g_2(q_v, \tau; t) = \frac{1}{b f_\infty}\big(\langle C(q_v, t_1, t_1 + \tau)\rangle_{t_1} - 1\big), \qquad (2)$$

where the average is over a small interval of t_1 so that the autocorrelation function can be considered an approximate snapshot of the dynamics, and the waiting time t is taken as the mean value of t_1 over the interval. Specifically, since the dynamics evolved during the measurement, the length of the interval was chosen to balance two conflicting priorities: (i) it needed to be large enough that $\Delta g_2(q_v, \tau; t)$ decayed sufficiently to characterize the dynamics, but (ii) it needed to be short enough so that $\Delta g_2(q_v, \tau; t)$ at different t resolved the waiting-time dependence of the dynamics. As an illustration of the chosen procedure, Fig. 3 shows the region, bounded by the white parallelogram, of the instantaneous correlation function that was included in calculating $\Delta g_2(q_v, \tau; t)$ at $t =$ 293 s from the measurement at 6% strain. The horizontal and vertical arrows indicating the extent of the regions have length $\Delta t = 5t/6$, which was found to be optimal for balancing the above criteria. This sized region relative to t (i.e., $\Delta t = 5t/6$) was employed in calculating $\Delta g_2(q_v, \tau; t)$ at all waiting times.

Figure 5(a) shows a set of autocorrelation functions for $\gamma = 6\%$. With increasing waiting time, $\Delta g_2(q_v, \tau; t)$ decays at a larger τ, reflecting the steadily slowing microscopic dynamics along the initial flow direction. However, the autocorrelation functions at different t maintain the same shape, indicating that the qualitative nature of the dynamics did not change with waiting time. The autocorrelation functions at different q_v also have very similar shapes, so that $\Delta g_2(q_v, \tau; t)$ at all q_v and t collapse onto a master curve when τ is scaled by the product of a wave-vector-dependent factor $\alpha(q_v)$ and a waiting-time-dependent factor $\delta(t)$, as shown in Fig. 5(b). As shown in the inset to Fig. 5(b), $\alpha(q_v) \sim q_v$. The same lineshape and scaling behavior of $\Delta g_2(q_v, \tau; t)$ was observed during stress relaxation at all strains. This scaling behavior contrasts with that expected for diffusive motion, for which $\alpha(q_v) \sim q_v^2$ perhaps modulated by the structure factor due to de Gennes narrowing [34]. Instead, it indicates the dynamics during the stress relaxation were convective along the direction of the initial strain.

We interpret this convective motion as an ultra-slow, long-wavelength "backflow" in the glass and find that an affine velocity profile describes the observed dynamics very accurately. Specifically, we model the dynamics with a distribution of velocities in the direction opposite the initial strain [35] that varies linearly with distance from the cell walls and reaches a maximum $\mathbf{v_o}(t)$ at a position y_p from the outer wall,

$$\mathbf{v}(t, y) = \begin{cases} \left(\frac{y}{y_p}\right)\mathbf{v_o}(t), & \text{if } 0 < y < y_p. \\ \left(\frac{H-y}{H-y_p}\right)\mathbf{v_o}(t), & \text{if } y_p < y < H. \end{cases} \qquad (3)$$

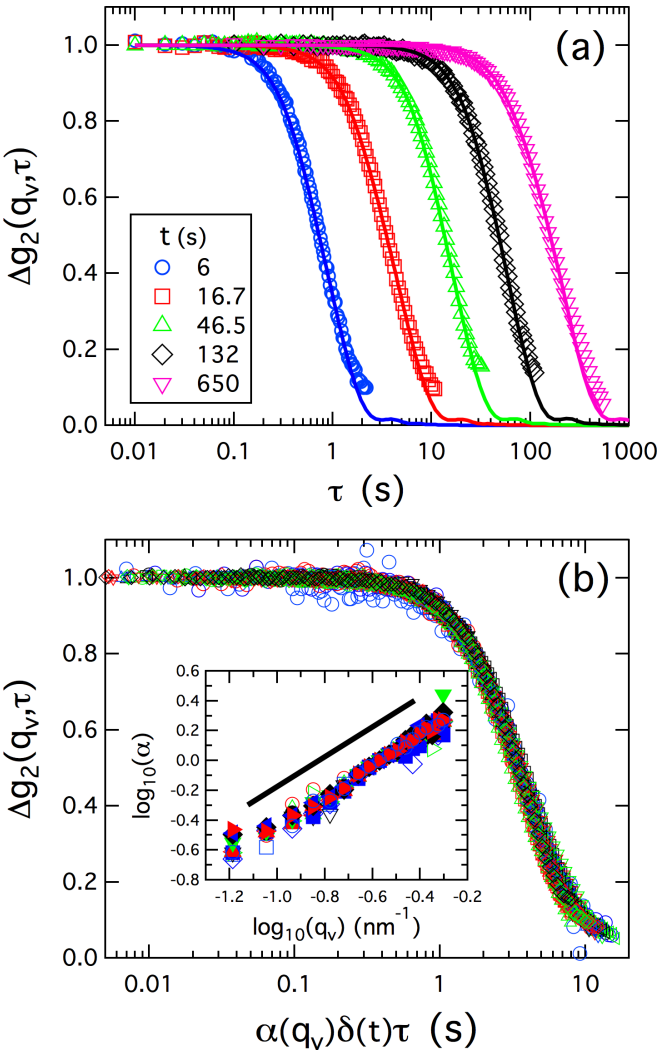

FIG. 5. (a) Normalized autocorrelation functions at $q_v = 0.26$ nm^{-1} along the flow direction at waiting times $t = 6$ (circles), 16.7 (squares), 46.5 (triangles), 132 (diamonds), and 650 s (inverted triangles) after a step to $\gamma = 6\%$. The solid lines show results of fits based on convective dynamics modeled using Eq. (4). (b) Autocorrelation functions at wave vectors 0.06 nm^{-1} $< q_v <$ 0.5 nm^{-1} and waiting times 6 s $< t <$ 500 s plotted against delay time scaled by a wave-vector-dependent factor $\alpha(q_v)$ and waiting-time-dependent factor $\delta(t)$. The inset shows $\log_{10}(\alpha)$ as a function of $\log_{10}(q_v)$. The solid line in the inset has a slope of one.

where y is the distance from the outer wall, and $H = 200\ \mu$m is the cell gap. The autocorrelation function for particle motion with such a velocity profile is given by [36,37]

$$\Delta g_2(\mathbf{q}, \tau) = \frac{\sin^2(q_v v_o \tau/2)}{(q_v v_o \tau/2)^2}. \qquad (4)$$

Because $\mathbf{v_o}$ varies with waiting time, and each measurement of $\Delta g_2(\mathbf{q}, \tau; t)$ spans a range of t, we fit the data by integrating Eq. (4) over a range of $\mathbf{v_o}$; details are provided in Appendix A. The solid lines in Fig. 5(a) show the results of such fits. The agreement between the fits and the data is essentially perfect, but we note that $\Delta g_2(\mathbf{q}, \tau)$ depends only on the distribution of particle velocities parallel to $\mathbf{q}$ in the

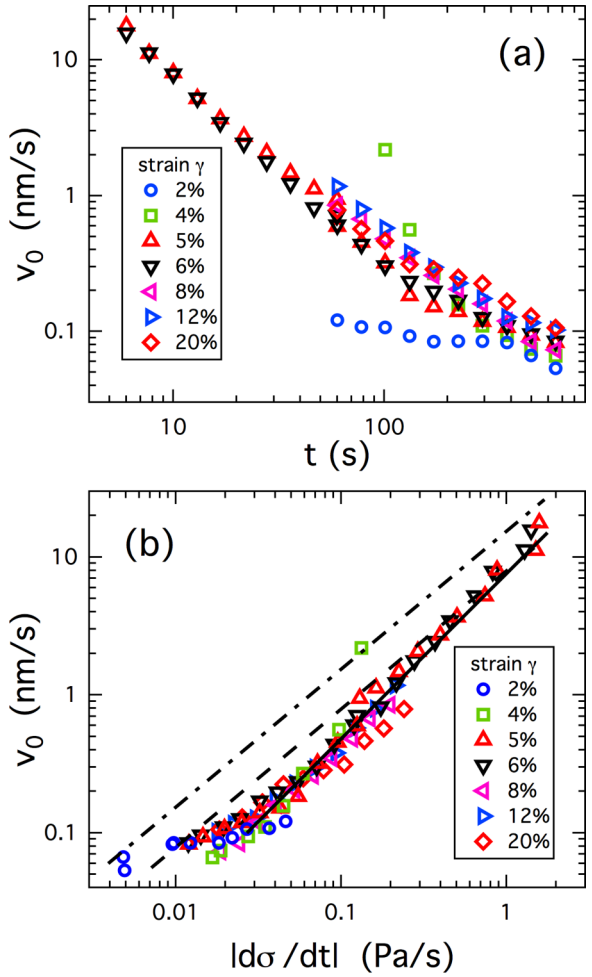

FIG. 6. (a) Peak velocity of convective motion as a function of waiting time following step strains of sizes specified in the legend. (b) Peak velocity as a function of the rate of change of the stress. The solid line shows the result of a power-law fit, $v_o \sim |d\sigma/dt|^m$, to the data with $v_o > 0.1$ nm/s, which gives $m = 1.20 \pm 0.01$. The dashed and dash-dotted lines show the relations $v_o = \frac{H}{2G'}|d\sigma/dt|$ and $v_o = \frac{H}{G'}|d\sigma/dt|$, respectively, where $G' = 13$ kPa approximates the linear elastic modulus of the glass and H is the cell gap.

scattering volume [38], and hence Eq. (4) is independent of y_p. That is, velocity profiles ranging from a symmetric triangular profile, $y_p = H/2$, to uniform shear due to a narrow slip plane near the inner cell wall, $y_p \approx H$, are indistinguishable. This ambiguity regarding the flow profile is further illustrated by an alternative analysis presented in Appendix B that shows a parabolic, Poiseuelle-like velocity profile models $\Delta g_2(\mathbf{q}, \tau; t)$ nearly as closely as Eq. (3) does. However, since XPCS measurements are especially sensitive to velocity differences across the scattering volume [36,38], the results for the peak velocity, whose magnitude v_o is shown in Fig. 6(a) as a function of waiting time for all the strains, are robust. As these results demonstrate, the convective flow slows steadily, with $v_o < 0.1$ nm/s at large t, but persists to the largest measurement times.

Figure 6(b) displays v_o for all the strains plotted against the rate of macroscopic stress decay $|d\sigma/dt|$ obtained from differentiating numerically the results in Fig. 1(b). The rate of convective motion scales with $|d\sigma/dt|$ irrespective of step size, demonstrating an intimate relationship between this motion and the stress relaxation. At early t, when v_o and $|d\sigma/dt|$ are large, the scaling approximates a power law, $v_o \sim |d\sigma/dt|^m$ with $m = 1.20 \pm 0.01$, as indicated by the solid line in Fig. 6(b), which shows the result of a power-law fit to the data with $v_o > 0.1$ nm/s. This slow convective motion and its persistent role in the stress relaxation contrasts with expectations based on simulations of soft glasses after shear cessation that identified a brief initial period of rapid ballistic motion followed by an extended period of local particle rearrangements [14,15].

An intriguing connection can be made with the linear elasticity of the glass that further indicates the significance of this convective motion and suggests a way to distinguish the position y_p of the velocity peak. In the linear regime at low strains in Fig. 1(a), $\sigma = G'\gamma$ with shear modulus $G' \approx 13$ kPa, or differentiating, $\dot{\sigma} = G'\dot{\gamma}$. Identifying effective shear rates to the velocity profile, $\dot{\gamma}_{\rm eff} = v_o/H$ if $y_p = H$ or $\dot{\gamma}_{\rm eff} = 2v_o/H$ if $y_p = H/2$, one arrives at $v_o = \frac{H}{G'}|d\sigma/dt|$ or $\frac{H}{2G'}|d\sigma/dt|$ for $y_p = H$ or $H/2$, respectively. These relations are shown by the dash-dotted and dashed lines in Fig. 6(b). The symmetric case, $y_p = H/2$, agrees better quantitatively with the data, suggesting the peak convective velocity was in the interior of the sample. This comparison with linear elasticity is only approximate, however, due to the nonlinear scaling of v_o with $|d\sigma/dt|$ at early t. We interpret this nonlinear scaling with $m > 1$ as evidence for strain softening of the glass as a result of the yielding.

B. Dynamics along the vorticity direction: Intermittent motion

Accompanying this persistent convection in the flow direction, along the vorticity direction intermittent, avalanchelike events dominate particle motion. For example, Fig. 7 shows the instantaneous correlation function at a wave vector along the vorticity direction, $q_\omega = 0.26$ nm^{-1}, during stress relaxation at $\gamma = 6\%$. In contrast to the steadily broadening profile in Fig. 3, $C(q_\omega, t_1, t_2)$ shows irregular changes that signify unsteady particle motion. For instance, as seen in Fig. 7, motion along the vorticity direction is largely arrested from $t \approx 350$ to ≈ 650 s, as $C(q_\omega, t_1, t_2)$ in this time range (i.e., both $350\,\text{s} < t_1 < 650$ s and $350\,\text{s} < t_2 < 650$ s) maintains a large, nearly constant value. However, near $t \approx 650$ s, a major rearrangement occurs so that speckle patterns prior to $t \approx 650$ s and after $t \approx 650$ s are largely uncorrelated. Additional events occur near $t \approx 240$ s and $t \approx 760$ s, as indicated by arrows in Fig. 7.

Figure 8 displays $C(q_\omega, t_1, t_2)$ measured in the vorticity direction at $q_\omega = 0.26$ nm^{-1} during stress relaxation measurements following steps to other strains. As with 6% strain, the dynamics are characterized by intermittent events involving large-scale particle rearrangements that lead to large decreases in the correlation functions. Avalanchelike events are well documented in disordered systems yielding under stress [22,23,39–43]. Here, we observe them associated with stress relaxation. We also note a similarity between these events and intermittent microscopic dynamics in aging colloidal and metallic glasses following quenches through the

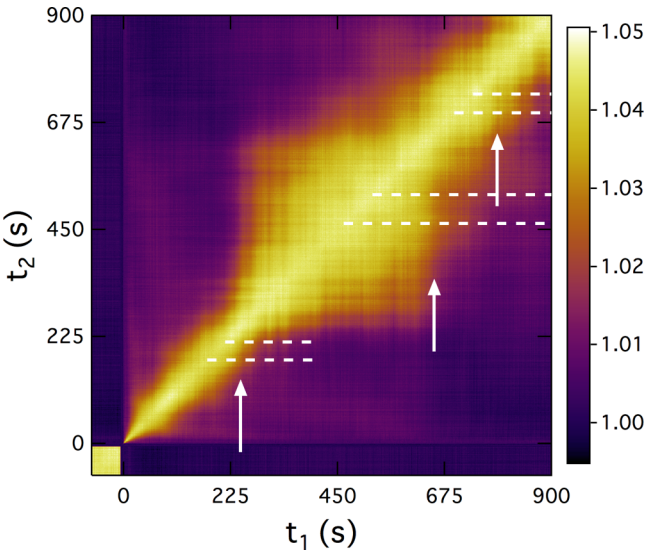

FIG. 7. Instantaneous correlation function $C(q_\omega, t_1, t_2)$ during a stress relaxation measurement following a step to $\gamma = 6\%$ at $q_\omega = 0.26\ \mathrm{nm}^{-1}$ along the vorticity direction. The arrows indicate waiting times at which intermittent events cause loss of correlation. The dashed lines show the boundaries of the regions over which averages were performed to obtain the correlation functions at fixed t_2 shown in Fig. 10.

glass transition [44,45], suggesting a connection between the microscopic dynamics of stress relaxation and aging.

These irregular decorrelations in $C(q_\omega, t_1, t_2)$ appear at all q_ω, but their precise positions in time vary with q_ω, providing information about the nature of the dynamics underlying the events. For example, Fig. 9 displays the instantaneous correlation function measured at various wave vectors in the vorticity direction during the stress relaxation measurement at $\gamma = 6\%$. To evaluate this wave-vector dependence quantitatively, we focus on the three events indicated by the arrows in Fig. 7 and identify the waiting times at which the instantaneous correlation falls to $1/e$ its maximum value in each case, a time we label t_d. We note that analysis of the intensity autocorrelation function $\Delta g_2(\mathbf{q}, \tau; t)$ is not appropriate for interpreting of such intermittent changes in correlation. Since τ is a time difference, and the calculation of $\Delta g_2(\mathbf{q}, \tau; t)$ averages over absolute time, $\Delta g_2(\mathbf{q}, \tau; t)$ should in principle not depend on absolute time, and in general it should be used only in the cases where the dynamics are steady-state such that no particular points in absolute time are special. (The use of $\Delta g_2(q_v, \tau; t)$ to analyze the dynamics in the flow direction described in Sec. III A above does not strictly adhere to this restriction; however, since those dynamics evolve slowly and smoothly, the deviations from steady state can be accounted for straightforwardly when interpreting the correlation functions.) Instead, to identify quantitatively the waiting time of the events that lead to loss of correlation in $C(q_\omega, t_1, t_2)$ at $\gamma = 6\%$ near $t \approx 650$ s, we plot in Fig. 10(a) $C(q_\omega, t_1, t_2)$ at a fixed t_2 that is earlier than the time of the event ($t_2 < 650$ s) as a function of t_1 for several q_ω. Specifically, to improve statistics we plot the average of $C(q_\omega, t_1, t_2)$ over a small range of t_2 demarcated by the dashed lines in Fig. 7, $462\ \mathrm{s} < t_2 < 523$ s, versus t_1. This correlation function hence displays how correlation in the speckle patterns is lost as the event near $t \approx 650$ s progresses. The correlation function decays over a

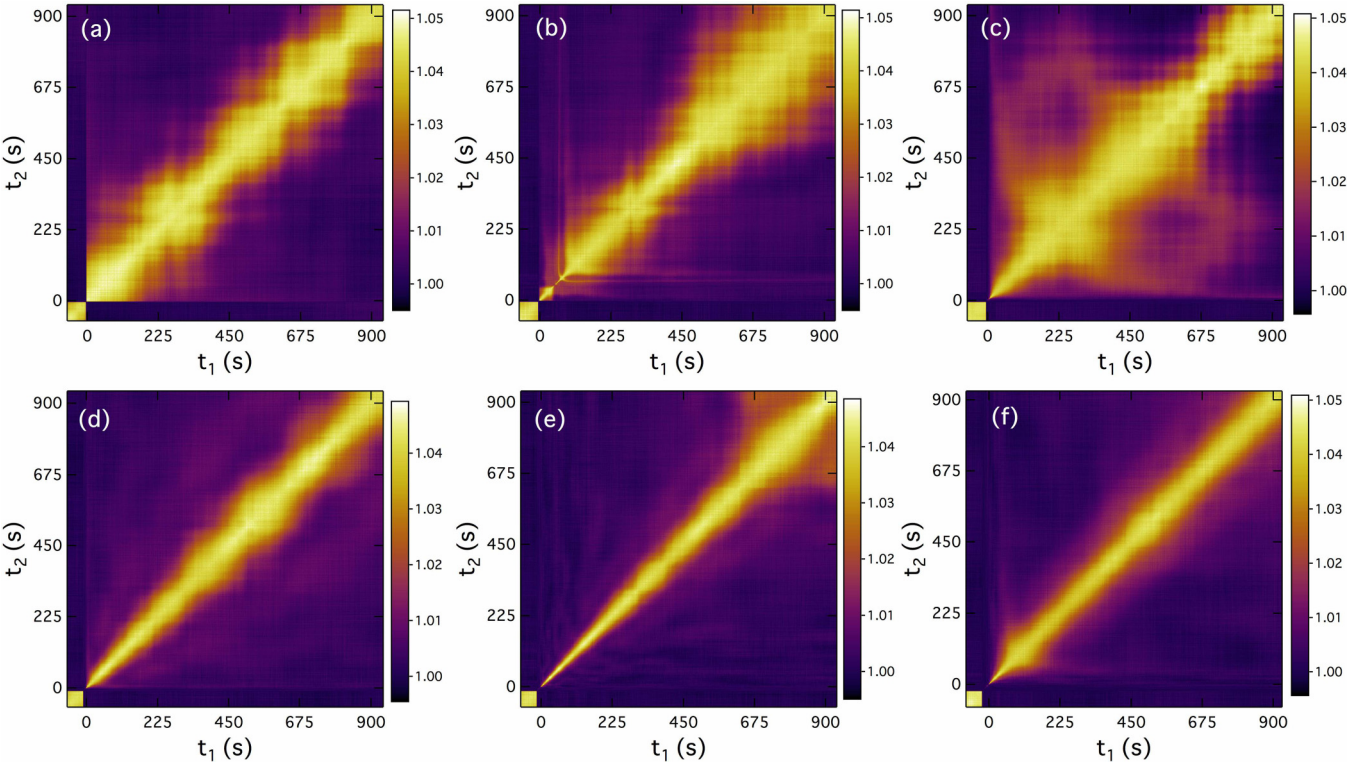

FIG. 8. Instantaneous correlation function $C(q_\omega, t_1, t_2)$ during stress relaxation measurements following steps to strains of (a) 2%, (b) 4%, (c) 5%, (d) 8%, (e) 12%, and (f) 20% measured at $q_\omega = 0.26\ \mathrm{nm}^{-1}$ along the vorticity direction, perpendicular of the initial strain.

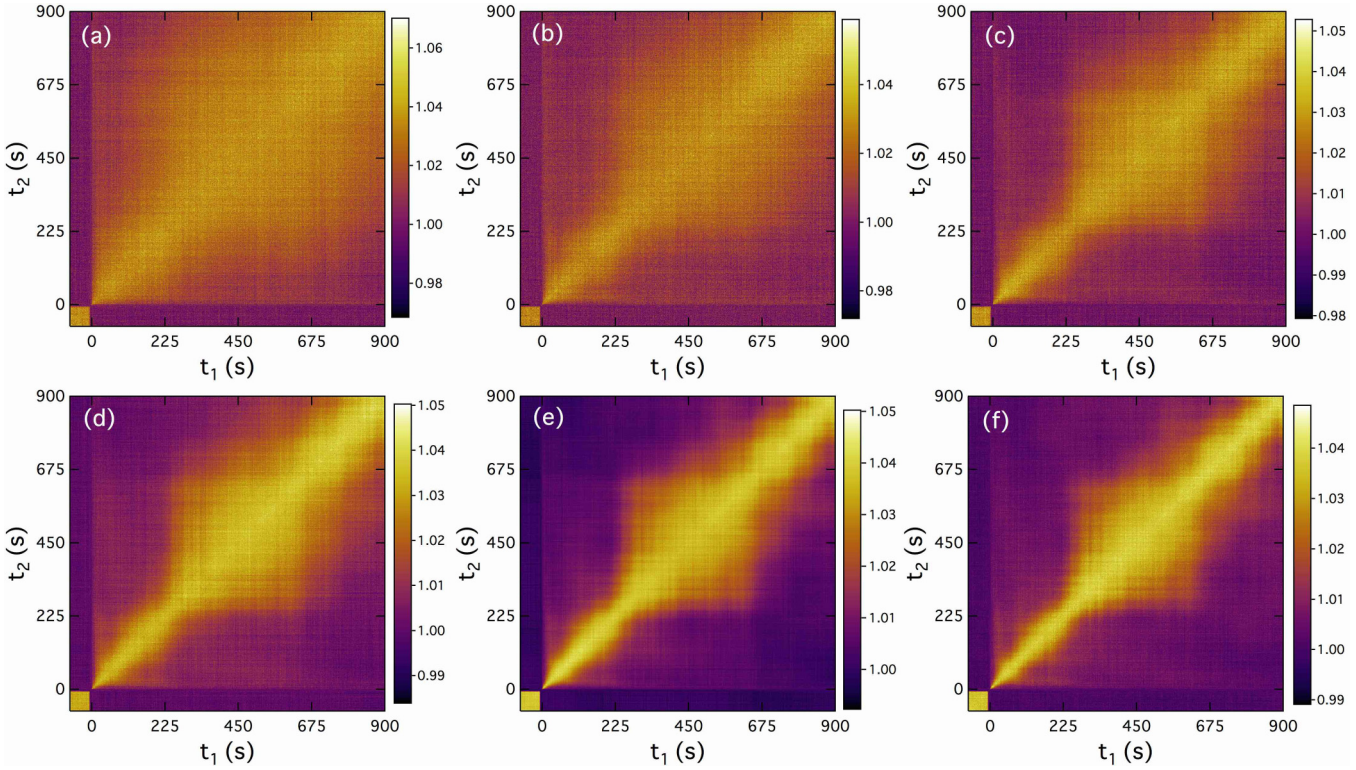

FIG. 9. Instantaneous correlation function $C(q_\omega, t_1, t_2)$ during stress relaxation measurements following a step to strain of 6% measured along the vorticity direction at (a) $q_\omega = 0.09$, (b) 0.15, (c) 0.18, (d) 0.21, (e) 0.24, and (f) 0.30 nm^{-1}.

range of t_1 that depends on q_ω. We fit the decays to an empirical stretched-exponential lineshape, $\Delta C \exp\left(-(t_1/t_d)^\beta\right)$, where t_d can be considered the waiting time at which particle displacements during the event reached a length of order q_ω^{-1}. The results for t_d at different q_ω are shown in the inset Fig. 10(a). The time varies approximately linearly with wave vector, indicating the motion associated with the event is convective. The line in the inset shows the result of a linear fit, $t_d = t_{di} + (v_d q_\omega)^{-1}$, from which we find the convective motion initiates at waiting time $t_{di} = 534 \pm 10$ s and proceeds with characteristic velocity $v_d = 0.023 \pm 0.001$ nm/s.

Figures 10(b) and 10(c) display results of equivalent analysis of the drops in correlation seen in $C(q_\omega, t_1, t_2)$ in Fig. 7 near $t \approx 240$ and ≈ 760 s, respectively. Specifically, Fig. 10(b) shows $C(q_\omega, t_1, t_2)$ at a fixed t_2 below 240 s as a function of t_1 to capture the decorrelation at $t \approx 240$ s for several q_ω. To improve statistics the average of $C(q_\omega, t_1, t_2)$ over the narrow range 176 s $< t_2 <$ 213 s is shown versus t_1. The solid lines again show the results of fits using the same empirical lineshape, $\Delta C \exp\left(-(t_1/t_d)^\beta\right)$. Figure 10(c) displays the corresponding results and analysis for the decorrelation near $t \approx 760$ s. In this case, $C(q_\omega, t_1, t_2)$ averaged over the narrow range 695 s $< t_2 <$ 735 s is shown versus t_1. The insets to Figs. 10(b) and 10(c) display t_d as a function of q_ω^{-1} for each event. Again, t_d varies approximately linearly with q_ω^{-1}, as indicated by the lines in the insets. However, deviations from smooth linear behavior are also apparent in these events. We interpret these deviations as evidence that the motion associated with these events, while primarily convective, did not proceed smoothly but itself had some intermittency.

We interpret this intermittent convection in the vorticity direction as a consequence of the dense packing in the glass and the backflow along the flow direction. As the particles move relative to their neighbors as part of the back flow, their jammed, disordered arrangement necessitates motion in the transverse direction at irregular intervals. However, we emphasize that these events, which involve particle displacements primarily perpendicular to the initial strain, appear to be only indirectly related to the decay of the macroscopic stress. As Fig. 6(b) illustrates, the slow, steady motion that dominates dynamics in the flow direction is the microscopic process that couples most closely to the stress relaxation.

IV. CONCLUSION

In conclusion, this study employing XPCS with *in situ* rheometry has uncovered an unexpected microscopic process for stress relaxation in soft glasses associated with slow, persistent convective motion antiparallel to the preceding strain. We note this convection resembles flow seen previously in filled polymers following tensile step strains [46]. This similarity suggests this mechanism for stress relaxation might be general to amorphous solids. This observation also further suggests connections with spontaneous slow dynamics seen in previous XPCS and dynamic light scattering (DLS) experiments on systems that have undergone rapid gelation [47–52]. Those dynamics, which similarly persist long after solidification and have the same scaling with wave vector as in the inset to Fig. 5(b), have been tentatively interpreted as heterogeneous strain related to slow relaxation of internal

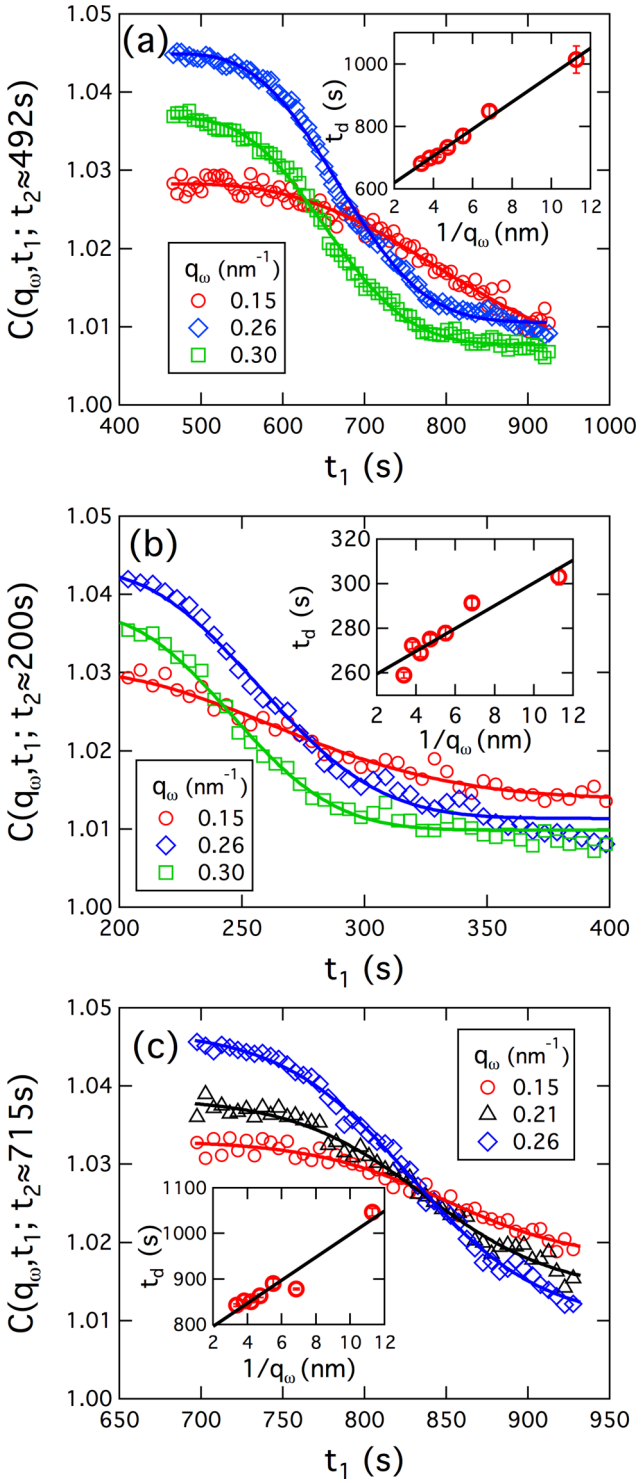

FIG. 10. Analysis of the drops in correlation in $C(q_\omega, t_1, t_2)$ near (a) $t \approx 650$, (b) ≈ 240, and (c) ≈ 760 s during the stress relaxation measurement at $\gamma = 6\%$. (a) shows $C(q_\omega, t_1, t_2)$ averaged over the narrow range, 462 s $< t_2 <$ 523 s, as a function of t_1 at $q_\omega = 0.15$ (circles), 0.26 (diamonds), 0.30 nm^{-1} (squares). The lines through the data show the results of fits described in the text to find the waiting time t_d of the drop in correlation. As shown in the inset, t_d varies linearly with q_ω^{-1}. (b) shows the equivalent analysis of $C(q_\omega, t_1, t_2)$ averaged over the narrow range 176 s $< t_2 <$ 213 s as a function of t_1 and (c) shows equivalent analysis over the range 695 s $< t_2 <$ 735 s.

stresses [53]. Further studies that interrogate the microscopic dynamics associated with stress relaxation in glassy materials would help illuminate these issues. More broadly, the capability demonstrated here of integrating rheometry with XPCS, particularly when combined with recent advances incorporating DLS with mechanical measurements [54,55], holds promise for measuring the dynamics at the origin of a host of nonlinear rheological behavior in soft materials over a broad range of lengths down to the nanometer scale.

ACKNOWLEDGMENTS

Funding was provided by the NSF (CBET-1804721) and the NSERC Discovery grant program. The research used resources of the Advanced Photon Source and the Center for Nanoscale Materials, US Department of Energy (DOE) Office of Science User Facilities operated for the DOE Office of Science by Argonne National Laboratory under Contract No. DE-AC02-06CH11357.

APPENDIX A: FITTING $\Delta g_2(q_v, \tau; t)$

As described above, the process of obtaining $\Delta g_2(q_v, \tau; t)$ from $C(q_v, t_1, t_2)$ involved averaging over the waiting-time interval Δt. Hence, the measured $\Delta g_2(q_v, \tau; t)$ was related to the "actual" time-varying autocorrelation function $\Delta g_2^a(q_v, \tau; t)$ by

$$\Delta g_2(q_v, \tau; t) = \frac{1}{\Delta t} \int_{t-\Delta t/2}^{t+\Delta t/2} \Delta g_2^a(q_v, \tau; t')dt' \qquad \text{(A1)}$$

In the model of convective flow, Eqs. (3) and (4), $\Delta g_2(q_v, \tau; t)$ depends on the peak velocity v_0, which varies with waiting time. To fit the data using the model, we hence converted the integral in Eq. (A1) to an integral over peak velocities,

$$\Delta g_2(q_v, \tau; t) = A(v_l, v_h) \int_{v_l}^{v_h} \frac{\sin^2(q_v v_o t/2)}{(q_v v_o t/2)^2} p(v_0) dv_0, \qquad \text{(A2)}$$

where $v_l = v_0(t + \Delta t/2)$ and $v_h = v_0(t - \Delta t/2)$, $p(v_0)$ is a density function, and $A(v_l, v_h) = 1/\int_{v_l}^{v_h} p(v_0)dv_0$ is a normalization factor. To obtain a form for the density function needed to close this expression, we first noted that the characteristic decay time of $\Delta g_2(q_v, \tau; t)$ at any t should vary inversely with the velocity at that t. Hence, the waiting-time dependence of the velocity should vary approximately proportionally with the factor $\delta(t)$ that rescales τ such that $\Delta g_2(q_v, \tau; t)$ at different t collapse onto a single scaling function as shown in Fig. 5(b). Figure 11 shows $\delta(t)$ for all of the strain amplitudes and waiting times. The scale factor decays at early waiting times approximately as a power law, $\delta(t) \sim t^d$, where the exponent varies slightly with strain but in all cases is roughly $d = -1.2$. Hence, for the purposes of approximating $p(v_0)$, we assumed the peak velocity had the same power-law relation with waiting time as $\delta(t)$, which leads to

$$p(v_0) \propto v_0^{\frac{1}{d}-1}. \qquad \text{(A3)}$$

With this form for $p(v_0)$, we fit Eq. (A2) to $\Delta g_2(q_v, \tau; t)$ with v_l and v_h as free parameters, leading to the fit results

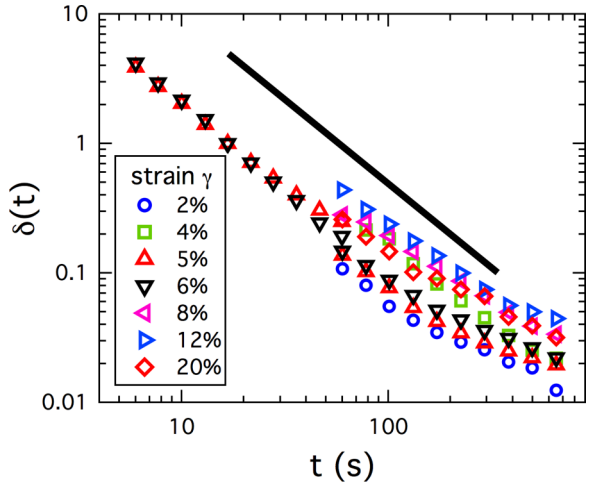

FIG. 11. Factors used to scale τ in order to collapse $\Delta g_2(q_v, \tau; t)$ at different waiting times like in Fig. 5(b). The correlation functions at all waiting times and all strains, as indicated in the legend, were scaled with respect to that for 6% strain at $t = 15$ s. Each value of δ is an average of the factors over wave vectors 0.024 nm$^{-1} < q <$ 0.030 nm^{-1}. The solid line depicts the power-law relation $\delta \sim t^{-1.2}$.

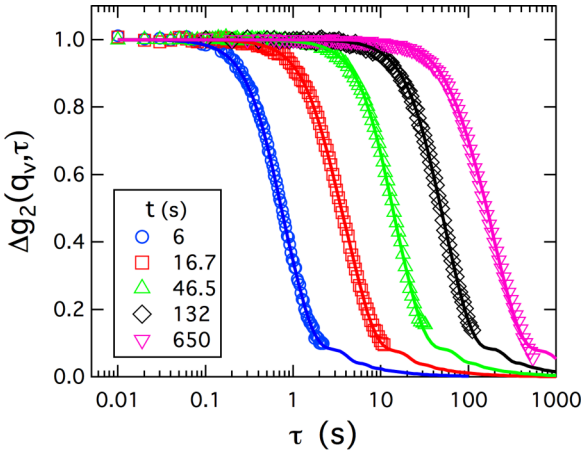

FIG. 12. Normalized autocorrelation functions at waiting times $t = 6$ (circles), 16.7 (squares), 46.5 (triangles), 132 (diamonds), and 650 s (inverted triangles) after a step to 6% strain. The solid lines show results of fits based on convective dynamics modeled by the parabolic velocity profile given in Eq. (B1).

shown in Fig. 5(a). Using the fitted values of v_l and v_h, we obtained the peak velocity for a given waiting time from

$$v_0(t) = A(v_l, v_h) \int_{v_l}^{v_h} v p(v_0) dv_0, \tag{A4}$$

leading to the values of v_0 shown in Fig. 6.

APPENDIX B: ALTERNATIVE MODEL FOR CONVECTIVE "BACK FLOW"

As an alternative to the linear velocity profile described above [Eq. (3)] to analyze $\Delta g_2(q_v, \tau; t)$, we consider here a velocity profile with a parabolic shape analogous to pressure-driven Poiseuille flow. Specifically, we model the particle dynamics with a velocity $\mathbf{v}$ in the direction opposite the initial strain that varies with distance y from the center of the cell gap as

$$\mathbf{v}(t, y) = -\mathbf{v_p}(t)\left(1 - \frac{4y^2}{H^2}\right), \tag{B1}$$

where $\mathbf{v_p}(t)$ is the peak velocity, oriented in the flow direction, and $H = 200$ μm is the cell gap. The autocorrelation function for particle motion with such a velocity profile is given by [37]

$$\Delta g_2(\mathbf{q}, \tau) = \frac{1}{\omega\tau}[C^2(\sqrt{\omega\tau}) + S^2(\sqrt{\omega\tau})], \tag{B2}$$

where $\omega = \frac{2}{\pi}\mathbf{q} \cdot \mathbf{v_p}$, and $C(x)$ and $S(x)$ are Fresnel integrals. Following the same procedure as described in Appendix A to account for the time dependence of the velocity, we fit $\Delta g_2(q_v, \tau; t)$ using this model. Figure 12 shows $\Delta g_2(q_v, \tau; t)$ at different waiting times like in Fig. 5(a) along with results of these fits. As the figure indicates, the parabolic velocity profile models the data well; however, a quantitative comparison with the fits using the linear velocity profile shows that the linear profile gives better agreement with the data. The time-dependent peak velocities $v_p(t)$ that result from the fits with the parabolic profile are very similar to the time-dependent velocities describing the linear profiles $v_0(t)$ shown in Fig. 6, and so the same conclusions regarding the velocities can be made.

[1] D. Bonn, M. M. Denn, L. Berthier, T. Divoux, and S. Manneville, Yield stress materials in soft condensed matter, Rev. Mod. Phys. **89**, 035005 (2017).

[2] J. Boschan, D. Vågberg, E. Somfai, and B. P. Tighe, Beyond linear elasticity: Jammed solids at finite shear strain and rate, Soft Matter **12**, 5450 (2016).

[3] J. Boschan, S. A. Vasudevan, P. E. Boukany, E. Somfai, and B. P. Tighe, Stress relaxation in viscous soft spheres, Soft Matter **13**, 6870 (2017).

[4] G. Yin and M. J. Solomon, Soft glassy rheology model applied to stress relaxation of a thermoreversible colloidal gel, J. Rheol. **52**, 785 (2008).

[5] A. S. Negi and C. O. Osuji, Physical aging and relaxation of residual stresses in a colloidal glass following flow cessation, J. Rheol. **54**, 943 (2010).

[6] C. O. Osuji, C. Kim, and D. A. Weitz, Shear thickening and scaling of the elastic modulus in a fractal colloidal system with attractive interactions, Phys. Rev. E **77**, 060402(R) (2008).

[7] E. Moghimi, A. R. Jacob, and G. Petekidis, Residual stresses in colloidal gels, Soft Matter **13**, 7824 (2017).

[8] M. Ballauff, J. M. Brader, S. U. Egelhaaf, M. Fuchs, J. Horbach, N. Koumakis, M. Krüger, M. Laurati, K. J. Mutch, G. Petekidis, M. Siebenbürger, Th. Voigtmann, and J. Zausch, Residual Stresses in Glasses, Phys. Rev. Lett. **110**, 215701 (2013).

[9] P. Lidon, L. Villa, and S. Manneville, Power-law creep and residual stresses in a carbopol gel, Rheol. Acta **56**, 307 (2017).
[10] K. N. Pham, G. Petekidis, D. Vlassopoulos, S. U. Egelhaaf, W. C. K. Poon, and P. N. Pusey, Yielding behavior of repulsion- and attraction-dominated colloidal glasses, J. Rheol. **52**, 649 (2008).
[11] A. S. Negi and C. O. Osuji, Dynamics of internal stresses and scaling of strain recovery in an aging colloidal gel, Phys. Rev. E **80**, 010404(R) (2009).
[12] R. Bandyopadhyay, P. H. Mohan, and Y. M. Joshi, Stress relaxation in aging soft colloidal glasses, Soft Matter **6**, 1462 (2010).
[13] S. Fritschi, M. Fuchs, and Th. Voigtmann, Mode-coupling analysis of residual stresses in colloidal glasses, Soft Matter **10**, 4822 (2014).
[14] L. Mohan, R. T. Bonnecaze, and M. Cloitre, Microscopic Origin of Internal Stresses in Jammed Soft Particle Suspensions, Phys. Rev. Lett. **111**, 268301 (2013).
[15] L. Mohan, M. Cloitre, and R. T. Bonnecaze, Build-up and two-step relaxation of internal stress in jammed suspensions, J. Rheol. **59**, 63 (2015).
[16] M. E. A. Zakhari, M. Hütter, and P. D. Anderson, Stress relaxation of dense spongy-particle systems, J. Rheol. **62**, 831 (2018).
[17] J. Vermant and M. J. Solomon, Flow-induced structure in colloidal suspensions, J. Phys.: Condens. Matter **17**, R187 (2005).
[18] N. Koumakis, M. Laurati, S. U. Egelhaaf, J. F. Brady, and G. Petekidis, Yielding of Hard-Sphere Glasses During Start-Up Shear, Phys. Rev. Lett. **108**, 098303 (2012).
[19] T. Sentjabrskaja, M. Hermes, W. C. K. Poon, C. D. Estrada, R. Castañeda Priego, S. U. Egelhaaf, and M. Laurati, Transient dynamics during stress overshoots in binary colloidal glasses, Soft Matter **10**, 6546 (2014).
[20] N. C. Keim and P. E. Arratia, Yielding and microstructure in a 2d jammed material under shear deformation, Soft Matter **9**, 6222 (2013).
[21] K. H. Nagamanasa, S. Gokhale, A. K. Sood, and R. Ganapathy, Experimental signatures of a nonequilibrium phase transition governing the yielding of a soft glass, Phys. Rev. E **89**, 062308 (2014).
[22] M. C. Rogers, K. Chen, L. Andrzejewski, S. Narayanan, S. Ramakrishnan, R. L. Leheny, and J. L. Harden, Echoes in x-ray speckles track nanometer-scale plastic events in colloidal gels under shear, Phys. Rev. E **90**, 062310 (2014).
[23] M. C. Rogers, K. Chen, M. J. Pagenkopp, T. G. Mason, S. Narayanan, J. L. Harden, and R. L. Leheny, Microscopic signatures of yielding in concentrated nanoemulsions under large-amplitude oscillatory shear, Phys. Rev. Mater. **2**, 095601 (2018).
[24] P. Ballesta, G. Petekidis, L. Isa, W. C. K. Poon, and R. Besseling, Wall slip and flow of concentrated hard-sphere colloidal suspensions, J. Rheol. **56**, 1005 (2012).
[25] T. Sentjabrskaja, P. Chaudhuri, M. Hermes, W. C. K. Poon, J. Horbach, S. U. Egelhaaf, and M. Laurati, Creep and flow of glasses: Strain response linked to the spatial distribution of dynamical heterogeneities, Sci. Rep. **5**, 11884 (2015).
[26] S. Aime, L. Ramos, and L. Cipelletti, Microscopic dynamics and failure precursors of a gel under mechanical load, Proc. Natl. Acad. Sci. USA **115**, 3587 (2018).
[27] A.-M. Philippe, D. Truzzolillo, J. Galvan-Myoshi, P. Dieudonné-George, V. Trappe, L. Berthier, and L. Cipelletti, Glass transition of soft colloids, Phys. Rev. E **97**, 040601(R) (2018).
[28] D. Pennicard, S. Lange, S. Smoljanin, J. Becker, H. Hirsemann, M. Epple, and H. Graafsma, Development of LAMBDA: Large area medipix-based detector array, J. Instrum. **6**, C11009 (2011).
[29] F. Khan, S. Narayanan, R. Sersted, N. Schwarz, and A. Sandy, Distributed X-ray photon correlation spectroscopy data reduction using Hadoop *MapReduce*, J. Synchrotron Radiat. **25**, 1135 (2018).
[30] F. Scheffold and T. G. Mason, Scattering from highly packed disordered colloids, J. Phys.: Condens. Matter **21**, 332102 (2009).
[31] A. Madsen, R. L. Leheny, H. Guo, M. Sprung, and O. Czakkel, Beyond simple exponential correlation functions and equilibrium dynamics in x-ray photon correlation spectroscopy, New J. Phys. **12**, 055001 (2010).
[32] The Siegert factor measured using a thin Aerogel sample was approximately 0.11. Because in the rheo-XPCS measurements the scattering from the front and back of the Couette cell add incoherently, the Siegert factor is reduced effectively by a factor of 2.
[33] W. van Megen, S. M. Underwood, and P. N. Pusey, Nonergodicity Parameters of Colloidal Glasses, Phys. Rev. Lett. **67**, 1586 (1991).
[34] P. N. Segrè and P. N. Pusey, Scaling of the Dynamic Scattering Function of Concentrated Colloidal Suspensions, Phys. Rev. Lett. **77**, 771 (1996).
[35] The measurements do not distinguish whether the velocity is parallel or antiparallel to the imposed strain, but the assumption that it is antiparallel seems safe since the alternative is unphysical. Specifically, system is noninertial, so once the externally imposed strain rate is set to zero, any motion in the strain direction should cease essentially immediately. Any continued, internally driven motion in that direction would increase the stress.
[36] W. R. Burghardt, M. Sikorski, A. R. Sandy, and S. Narayanan, X-ray photon correlation spectroscopy during homogenous shear flow, Phys. Rev. E **85**, 021402 (2012).
[37] J. R. M. Lhermitte, M. C. Rogers, S. Manet, and M. Sutton, Velocity measurement by coherent x-ray heterodyning, Rev. Sci. Instrum. **88**, 015112 (2017).
[38] R. L. Leheny, M. C. Rogers, K. Chen, S. Narayanan, and J. L. Harden, Rheo-XPCS, Curr. Opin. Colloid Interface Sci. **20**, 261 (2015).
[39] D. M. Dimiduk, C. Woodward, R. LeSar, and M. D. Uchic, Scale-free intermittent flow in crystal plasticity, Science **312**, 1188 (2006).
[40] N. P. Bailey, J. Schiøtz, A. Lemaître, and K. W. Jacobsen, Avalanche Size Scaling in Sheared Three-Dimensional Amorphous Solid, Phys. Rev. Lett. **98**, 095501 (2007).
[41] J. Antonaglia, W. J. Wright, X. Gu, R. R. Byer, T. C. Hufnagel, M. LeBlanc, J. T. Uhl, and K. A. Dahmen, Bulk Metallic Glasses Deform Via Slip Avalanches, Phys. Rev. Lett. **112**, 155501 (2014).
[42] K. M. Salerno, C. E. Maloney, and M. O. Robbins, Avalanches in Strained Amorphous Solids: Does Inertia Destroy Critical Behavior? Phys. Rev. Lett. **109**, 105703 (2012).

[43] K. E. Daniels and N. W. Hayman, Force chains in seismogenic faults visualized with photoelastic granular shear experiments, J. Geophys. Res. **113**, B11411 (2008).

[44] E. Wandersman, A. Duri, A. Robert, E. Dubois, V. Dupuis, and R. Perzynski, Probing heterogeneous dynamics of a repulsive colloidal glass by time resolved x-ray correlation spectroscopy, J. Phys.: Condens. Matter **20**, 155104 (2008).

[45] Z. Evenson, B. Ruta, S. Hechler, M. Stolpe, E. Pineda, I. Gallino, and R. Busch, X-Ray Photon Correlation Spectroscopy Reveals Intermittent Aging Dynamics in a Metallic Glass, Phys. Rev. Lett. **115**, 175701 (2015).

[46] F. Ehrburger-Dolle, I. Morfin, F. Bley, F. Livet, G. Heinrich, S. Richter, L. Piché, and M. Sutton, XPCS investigation of the dynamics of filler particles in stretched filled elastomers, Macromolecules **45**, 8691 (2012).

[47] L. Cipelletti, S. Manley, R. C. Ball, and D. A. Weitz, Universal Aging Features in the Restructuring of Fractal Colloidal Gels, Phys. Rev. Lett. **84**, 2275 (2000).

[48] L. Ramos and L. Cipelletti, Ultraslow Dynamics and Stress Relaxation in the Aging of a Soft Glassy System, Phys. Rev. Lett. **87**, 245503 (2001).

[49] B. Chung, S. Ramakrishnan, R. Bandyopadhyay, D. Liang, C. F. Zukoski, J. L. Harden, and R. L. Leheny, Microscopic Dynamics of Recovery in Sheared Depletion Gels, Phys. Rev. Lett. **96**, 228301 (2006).

[50] H. Guo, S. Ramakrishnan, J. L. Harden, and R. L. Leheny, Gel formation and aging in weakly attractive nanocolloid suspensions at intermediate concentrations, J. Chem. Phys. **135**, 154903 (2011).

[51] D. Orsi, B. Ruta, Y. Chushkin, A. Pucci, G. Ruggeri, G. Baldi, T. Rimoldi, and L. Cristofolini, Controlling the dynamics of a bidimensional gel above and below its percolation transition, Phys. Rev. E **89**, 042308 (2014).

[52] B. Ruta, O. Czakkel, Y. Chushkin, F. Pignon, R. Nervo, F. Zontone, and M. Rinaudo, Silica nanoparticles as tracers of the gelation dynamics of a natural biopolymer physical gel, Soft Matter **10**, 4547 (2014).

[53] L. Cipelletti, L. Ramos, S. Manley, E. Pitard, D. A. Weitz, E. E. Pashkovski, and M. Johansson, Universal non-diffusive slow dynamics in aging soft matter, Faraday Discuss. **123**, 237 (2003).

[54] N. Ali, D.C.D. Roux, L. Cipelletti, and F. Caton, Rheospeckle: A new tool to investigate local flow and microscopic dynamics of soft matter under shear, Meas. Sci. Technol **27**, 125902 (2016).

[55] S. Aime and L. Cipelletti, Probing shear-induced rearrangements in fourier space. I. dynamic light scattering, Soft Matter **15**, 200 (2019).